AGU PUBLICATIONS

Geochemistry, Geophysics, Geosystems

RESEARCH ARTICLE
10.1002/2017GC006937

The origin of volatiles in the Earth's mantle

Saswata Hier-Majumder[1] and Marc M. Hirschmann[2]

[1]Department of Earth Sciences, Royal Holloway University of London, Egham, UK, [2]Department of Earth Sciences, University of Minnesota, Minneapolis, Minnesota, USA

Key Points:
- Magma ocean freezing fronts retain more melt than previously thought
- Melt thus retained in the residual mantle can dissolve substantial amount of volatiles
- Following solidification of the magma ocean, the residual mantle can contain substantially larger amount of volatiles

Supporting Information:
- Supporting Information S1

Correspondence to:
S. Hier-Majumder,
saswata.hier-majumder@rhul.ac.uk

Citation:
Hier-Majumder, S., and M. M. Hirschmann (2017), The origin of volatiles in the Earth's mantle, *Geochem. Geophys. Geosyst.*, *18*, doi:10.1002/2017GC006937.

Received 24 MAR 2017
Accepted 11 JUL 2017
Accepted article online 26 JUL 2017

Abstract The Earth's deep interior contains significant reservoirs of volatiles such as H, C, and N. Due to the incompatible nature of these volatile species, it has been difficult to reconcile their storage in the residual mantle immediately following crystallization of the terrestrial magma ocean (MO). As the magma ocean freezes, it is commonly assumed that very small amounts of melt are retained in the residual mantle, limiting the trapped volatile concentration in the primordial mantle. In this article, we show that inefficient melt drainage out of the freezing front can retain large amounts of volatiles hosted in the trapped melt in the residual mantle while creating a thick early atmosphere. Using a two-phase flow model, we demonstrate that compaction within the moving freezing front is inefficient over time scales characteristic of magma ocean solidification. We employ a scaling relation between the trapped melt fraction, the rate of compaction, and the rate of freezing in our magma ocean evolution model. For cosmochemically plausible fractions of volatiles delivered during the later stages of accretion, our calculations suggest that up to 77% of total H_2O and 12% of CO_2 could have been trapped in the mantle during magma ocean crystallization. The assumption of a constant trapped melt fraction underestimates the mass of volatiles in the residual mantle by more than an order of magnitude.

Plain Language Summary The Earth's deep interior contains substantial amounts of volatile elements like C, H, and N. How these elements got sequestered in the Earth's interior has long been a topic of debate. It is generally assumed that most of these elements escaped the interior of the Earth during the first few hundred thousand years to create a primitive atmosphere, leaving the mantle reservoir nearly empty. In this work, we show that the key to this paradox involves the very early stages of crystallization of the mantle from a global magma ocean. Using numerical models, we show that the mantle stored substantially higher amounts of volatiles than previously thought, thanks to large quantities of melt trapped in the mantle due to rapid freezing of the magma ocean. Our models show that up to 77% of the total planetary budget of water and 12% of CO_2 can be stored in the mantle due to this previously unaccounted process.

1. Introduction

The distribution of major volatiles (H, C, N) between the Earth's principal reservoirs, the mantle, exosphere, and core has great influence on both surface and interior dynamics [*Hirschmann*, 2006; *Dasgupta and Hirschmann*, 2010; *McGovern and Schubert*, 1989; *Sleep and Zahnle*, 2001; *Hayes and Waldbauer*, 2006; *Rüpke et al.*, 2004]. An outstanding problem in understanding Earth's deep volatile cycles, however, is the initial conditions resulting from the evolution of the terrestrial magma ocean (MO). During the very early stages of the Earth's history, the abundances of these volatile species in the different reservoirs were determined by the coupled evolution of the magma ocean and the primitive atmosphere [*Abe and Matsui*, 1988; *Elkins-Tanton*, 2008; *Hamano et al.*, 2013]. As the magma ocean crystallized, incompatible volatiles were released to form a thick primitive greenhouse atmosphere, which subsequently slowed down the crystallization rate of the magma ocean. Recent evidence of isotopically light carbon inclusions in detrital zircon indicates that liquid water and biogenic carbon might have been present on the surface of the Earth as early as 4.1 Ga ago, implying that magma ocean crystallization must have been a rapid process [*Bell et al.*, 2015].

In current models of MO crystallization, an enduring puzzle has been the origin of the mantle reservoir of major volatiles, as early loss to the primitive atmosphere could render the residual mantle virtually volatile-free [*Hamano et al.*, 2013]. Crucially, the present-day inventory of major volatiles, though imperfectly known, includes substantial reservoirs in the mantle. Estimates of the fraction of hydrogen, carbon, and nitrogen in

the bulk silicate Earth (BSE, the whole Earth except the core) that resides in the mantle range 38–93, 50–98, and 15–60%, respectively [*Hirschmann and Dasgupta*, 2009; *Sleep and Zahnle*, 2001; *Marty*, 2012; *Halliday*, 2013].

An important aspect of volatile content of the residual mantle involves the efficiency of retention of volatile-rich melt in the MO freezing front. Previous models of MO solidification paid relatively little attention to the retention of melt and dissolved volatiles within the compacting freezing front [*Elkins-Tanton*, 2008; *Hamano et al*., 2013; *Snyder et al*., 1992; *Suckale et al*., 2012; *Lebrun et al*., 2013]. Geochemical models of MO differentiation typically consider ideal fractional or equilibrium crystallization or alternatively assume that a constant small (1–5%) [*Elkins-Tanton*, 2008; *Snyder et al*., 1992] fraction of melt is trapped. The assumption that a relatively small volume fraction of melt is trapped in the residual mantle leads to a relatively volatile depleted mantle upon the completion of the MO crystallization.

The amount of melt trapped in the crystal cumulates has great implications for the volatile content of the residual mantle. As the volatiles dissolve preferentially in the melt, higher fraction of melt trapped in the residual mantle will lead to an increase in its trapped volatile content. Upon further cooling, the melt will be trapped in volatile-free silicates as inclusions, crystallize into volatile-rich accessory minerals, or occur along grain boundaries. This effect is particularly important for the lower mantle, where the solubility of volatiles in the crystal structure of nominally volatile-free mineral phases is relatively small [*Bolfan-Casanova*, 2000, 2002; *Shcheka et al*., 2006]. For example, based on cosmochemical constraints, *Marty* [2012] estimates that the mantle contains ∼3000 ppm H_2O and ∼500 ppm C. In contrast, laboratory measurements indicate that the lower mantle phases such as magnesiowustite dissolve only up to 20 ppm of H_2O [*Bolfan-Casanova*, 2002], upper mantle silicates dissolve 12 ppm or less of C, and the C concentration in transition zone and lower mantle phases are less than 30–200 ppb [*Shcheka et al*., 2006]. This discrepancy in estimated reservoir size of the mantle volatiles and their low solubility in the silicate mineral structures can be reconciled by the presence of a volatile-rich trapped melt resulting from crystallization of the MO. Upon cooling, this trapped melt can result in solid carbonates and carbonate-rich melts in the upper mantle [*Hier-Majumder and Tauzin*, 2017] and diamond and metal carbides in the mid and lower mantle as storage sites of mantle C [*Dasgupta and Hirschmann*, 2010].

Solidification and melt entrapment in crystallizing terrestrial magma chambers provide smaller-scale natural analogs to MO crystallization. Such studies of layered mafic intrusions have long documented that melt extraction from crystallizing cumulate mushes can be inefficient [*Wager*, 1960; *Irvine*, 1980; *Cawthorn and Walraven*, 1998], sequestering up to 40% melt and dissolved incompatible elements in the residuum [*Tegner et al*., 2009]. As the rate of crystallization increases, these studies indicate that the volume fraction of trapped melt also increases. Typical solidification rates for layered mafic intrusions are on the order of 1–5 cm/yr [*Cawthorn and Walraven*, 1998], much slower than typical magma ocean solidification rates of 10 cm to a few meters per year [*Hamano et al*., 2013; *Elkins-Tanton*, 2008]. The ratio between the rate of crystallization and characteristic velocity of the matrix during compaction is an indicator of the efficiency of melt trapping, a higher value of the ratio indicating a higher volume fraction of melt trapped. Following our dimensionalization scheme outlined in supporting information section S1 and Table S1, the characteristic velocity of compaction within the mushy layer is ∼1 cm/yr. The ratio of the two velocities, therefore, are between 5 and 10 for magma chambers and between 10 and 100 for magma oceans. This simple scaling indicates that the freezing front of the MO should be at least as efficient as the magma chambers in retaining interstitial melt upon rapid freezing.

The amount of volatile stored through trapped interstitial melt in the residual mantle arises from a competition between two processes operating at two distinct length scales. On a global scale, crystallization of the terrestrial MO depends on the surface heat flux, modulated by the mass of greenhouse gases in the overlying primitive atmosphere; the shape of the solidus and the liquidus curves; and the latent heat of crystallization. Combination of these processes control the rate of cooling of the MO and the rate of evolution of the sizes of the reservoirs. In the scale of the freezing front, the volatile content is controlled by the volume fraction of melt trapped within the compacting matrix. This volume fraction, in turn, is controlled by the efficiency of compaction and melt expulsion from the freezing front. If the rate of MO crystallization is substantially slower than compaction, then the freezing front will be relatively depleted due to efficient melt expulsion from the freezing front. The situation will be reversed if the melt is frozen in-place due to

rapid rates of MO crystallization. The competition between these two distinct processes and their implications for the volatile content of the nascent mantle remains relatively poorly understood.

In this article, we address the dynamic coupling between the rate of magma ocean crystallization and volatile retention in the residual mantle by melt entrapment. To address the two different length scales of the problem, we first analyze the efficiency of melt expulsion in a compacting freezing front. This small-scale model leads to a parameterization of the trapped melt fraction as a function of competitions between rates of compaction and crystallization. Next, we combine this parameterization with a planetary-scale thermochemical evolution model. While the compaction and the thermochemical evolution models are not directly coupled, the parameterization serves as the link between them. In section 2, we discuss the formulations of these models in detail. In section 3, we present results for the evolution of the volatile masses in the three primary reservoirs, the MO, the primitive atmosphere, and the residual mantle. Finally, we discuss the implications of our results in section 4.

2. Model

The two models in this work are coupled by a parameterization of the melt fraction trapped in the residual mantle as a function of the characteristic time scale for compaction and the characteristic time scale for freezing. In section 2.1, we discuss the model of compaction within the freezing front followed by a detailed derivation of the thermal and chemical evolution equations in section 2.2.

In this article, we assume that the MO crystallizes bottom-up. The schematic diagram in Figure 1a outlines a schematic diagram of the model. The thickness of the freezing front is exaggerated for visibility. The three primary reservoirs, the residual mantle (RM), the magma ocean (MO), and the primitive atmosphere (PA) have the shape of concentric spherical shells. As the simulation proceeds, the sizes of the PA and RM increase while that of the MO decreases. In panel b, we outline a schematic diagram of the algorithm for the calculation. We start with a prescribed initial condition for the mantle potential temperature and volatile masses in the bulk, described in section 2.3. At each step of the iteration, we calculate the thermal structure within the MO to determine the depth of intersection of the MO adiabat and the freezing front (FF). Once the MO starts to crystallize, we also calculate the radius of the residual mantle and the rate of cooling-dependent trapped melt volume fraction at this stage. We then calculate the masses of each reservoir and their volatile content. Using this information, we quantify the pressure of the PA and the thermal emissivity of the atmosphere, which leads to the potential temperature for the next time step. Once the MO has crystallized completely, the

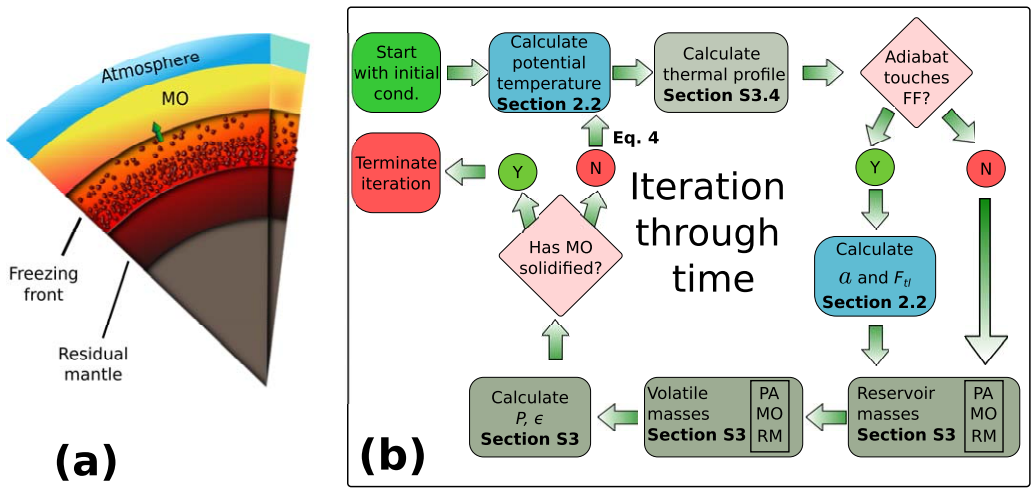

Figure 1. (a) A schematic diagram outlining the geometry of the freezing magma ocean. Notice that the thickness of the freezing front is exaggerated for clarity. (b) A schematic diagram outlining the algorithm for our simulations. Sections in the main article and the supporting information containing the details of these steps are indicated within the boxes. The initial conditions are described in section 2.3. Relevant equations in the boxes shaded in blue are discussed in the main article, while those in gray shaded boxes are discussed in supporting information.

iteration terminates. In the following subsections, we present the details involved in each of these steps. Additional details of the calculations are provided in supporting information.

2.1. Compaction Within the Freezing Front

As the magma ocean crystallizes, the compacting freezing front sweeps through the ocean, leaving the solidifying mantle behind. In this work, we define the freezing front in a rheological sense, such that the mineral grains are contiguous and form a load-bearing, viscous matrix, within which the melt is embedded in grain edge tubules. The boundary between the freezing front and the magma ocean is marked by the disaggregation melt fraction, at which the intergranular contact is lost leading to a sharp drop in the matrix viscosity [*Scott and Kohlstedt*, 2006; *Hier-Majumder et al*., 2006; *Wimert and Hier-Majumder*, 2012]. This definition of the freezing front implies that the front is a thin region of partial melt, with the melt volume fraction varying from 1 atop the front to 0.3 at the bottom. *Solomatov and Stevenson* [1993a] discussed the idea of a "rheological front" of a crystallizing MO, which is different from a "solidification front," marked by the intersection between the MO adiabat and the solidus. The freezing front in this article is similar in nature to this "rheological front," with a small but finite thickness.

In a viscous matrix with interstitial melt, freezing and compaction are governed by three coupled partial differential equations conserving mass and momentum of the melt and matrix phases and conservation of concentration of components (such as dissolved volatiles) within each phase in the freezing front. The detailed derivations of these governing partial differential equations for multicomponent, multiphase flow can be found in a number of articles [*McKenzie*, 1984; *Bercovici et al*., 2001; *McKenzie*, 2011; *Rudge et al*., 2011; *Takei and Hier-Majumder*, 2009]. For the sake of brevity, we refer the reader to these articles for the detailed derivations. The details of our governing equations, initial and boundary conditions, and results are outlined in supporting information section S1.

2.2. Thermal and Chemical Evolution of the Magma Ocean

Next, we derive the governing equation for cooling of the magma ocean and the evolution of the concentration of dissolved volatiles in the three reservoirs; the magma ocean (MO), the residual mantle (RM), and the primitive atmosphere (PA). Similar to the two recent works by *Hamano et al*. [2013] and *Elkins-Tanton* [2008], we use a thermal evolution equation where the primitive atmosphere is treated as a gray body and the thermal emissivity depends on the concentration of the volatiles. The unique aspect of our model, however, is dynamically coupling the trapped melt volume fraction within the residual mantle with the cooling rate using the parameterization described in the following subsection.

2.2.1. Parameterization for Dynamic Melt Trapping

As originally outlined by *McKenzie* [2011], the volume fraction of the trapped melt, F_{tl}, depends on the ratio of time scales between two competing processes, compaction within the freezing front and the rate of freezing. Compaction within the freezing front leads to the expulsion of trapped melt, while rapid crystallization of the front freezes the melt in place, inhibiting expulsion.

In a reference frame within the freezing front, the rate at which melt fraction is trapped within the front can be defined as the gain in melt fraction minus volume change due to matrix compression. Using the mass conservation equations of two-phase flow, we get

$$F_{tl} = -\int_0^{\tau} \frac{\Gamma}{\rho} \mathrm{d}t, \tag{1}$$

where Γ is the dimensional volumetric crystallization rate, ρ is the density, and τ, the upper limit of the integral, is a characteristic time scale for compaction. The right-hand side of the equation arises from mass conservation within the melt, as outlined in supporting information section S2. The characteristic time scale τ can be considered as the ratio between the thickness of the compacting layer and the matrix sedimentation velocity [*McKenzie*, 2011]. As discussed in section 4.2, we test the end results for several different values of τ.

Next, we express the rate of crystallization as a function of the thermal state of the magma ocean. Following *McKenzie* [2011], we can write the rate of crystallization, Γ, as

$$\frac{\Gamma}{\rho} = \frac{\phi_c}{\Delta T} \frac{\mathrm{d}T}{\mathrm{d}t}, \tag{2}$$

where ϕ_c is the disaggregation melt fraction, ΔT (<0) is the depth-dependent difference between the solidus and the liquidus temperatures, and $\mathrm{d}T/\mathrm{d}t(<0)$ is the secular cooling rate of the magma ocean. Combining equation (1) with equation (2), and assuming that $\mathrm{d}T/\mathrm{d}t$ remains constant over the interval of the integration, we obtain the following expression for dynamically trapped melt fraction:

$$F_{tl} = -\frac{\phi_c \tau}{\Delta T}\frac{\mathrm{d}T}{\mathrm{d}t}. \tag{3}$$

Rapid crystallization, marked by a high negative value of $\mathrm{d}T/\mathrm{d}t$, leads to a high value of F_{tl}, while rapid compaction, indicated by a low value of τ leads to a lower value of F_{tl}. Knowing the rate of secular cooling at a given time, and the temperature contrast between the liquidus and the solidus at the depth corresponding to the freezing front, we evaluate F_{tl} at each time step.

The trapped melt volume fraction in equation (3) depends on the compaction time τ. We can define the compaction as the time taken for a unit volume of the matrix to travel across the length of the freezing front. The compaction time, then, is given by the ratio between the thickness of the freezing front and the velocity of matrix sedimentation. While it is difficult to know the thickness of the freezing front, we assume a value of 50 km, similar to the average present day crustal thickness. As discussed in detail in supporting information section S1, the characteristic velocity of matrix sedimentation is $\sim$1.2 cm/yr, leading to a characteristic compaction time of 4.35 Ma. In our calculations, we use a compaction time of 1.2 Ma, which, as discussed later, leads to a more conservative estimate of volatile retention in the mantle. We also carry out an additional series of simulations by varying the compaction time from 0.1 to 2.5 Ma. The sensitivity of the final results to the value of the compaction time is discussed in section 4.2.

2.2.2. Thermal Evolution

Consider the magma ocean with a potential temperature T overlying a crystalline spherical shell of thickness a, measured from the core-mantle boundary to the top of the crystallizing mantle. The secular cooling results from a balance between the latent heat of solidification, the surface heat flux, and the stellar heat flux, expressed as

$$\left[\rho C_P\left(\frac{R^3-a^3}{3}\right)-\rho T\Delta S a^2\frac{\mathrm{d}a}{\mathrm{d}T}\right]\frac{\mathrm{d}T}{\mathrm{d}t} = -R^2\left[\sigma\epsilon\left(T^4-T_\infty^4\right)-F_s\right], \tag{4}$$

where C_p is the heat capacity, R is the planetary radius, ΔS is the entropy of crystallization, $\mathrm{d}a/\mathrm{d}T$ is the rate of increase in a with cooling, σ is the Stefan-Boltzmann constant, ϵ is the thermal emissivity of the atmosphere, T_∞ is the temperature of the surrounding space, and F_s is the incoming solar heat flux. The term on the left-hand side arises from volumetric heat loss minus the latent heat released due to crystallization and the term on the right-hand side arises from loss of heat due to surface heat flux and warming of the planet by incoming solar heat flux. The thermal emissivity, ϵ, depends on the concentration of volatiles in the atmosphere, primarily H_2O and CO_2 [*Elkins-Tanton*, 2008]. We present the equations used to calculate the time and composition-dependent thermal emissivity in supporting information section S3.1.

Equation (4) needs to be supplemented with the radius of the mantle, a, and the mass of volatiles in the atmosphere to calculate the thermal emissivity, ϵ. The mantle radius a is calculated from the thermal structure in the MO at each time step, with known values of solidus and liquidus temperatures in the mantle. We use the solidus and liquidus from the work of *Monteux et al.* [2016]. While it is well known that small quantities of dissolved volatiles can reduce the solidus temperature significantly, studies of such volatile-induced solidus depression are currently unavailable for the lower mantle. Consequently, our solidus and liquidus correspond to a volatile free system.

We define the top of the freezing front as the intersection between the mantle adiabat and the isopleth for 30 vol. % melt, which marks the rheological boundary for the freezing front. Knowing the solidus and liquidus temperatures as functions of depth, we determine the temperature of the 30 vol. % isopleth, $T_{FF}(r)$, as

$$T_{FF}(r) = T_{sol}(r) + 0.3\Delta T(r), \tag{5}$$

where $T_{sol}(r)$ is the solidus temperature at radius r, and $\Delta T(r)$ is the difference between the liquidus and the solidus temperature at radius r. In using this formulation, we made the simplification that the volume fraction of the melt is the same as the mass fraction.

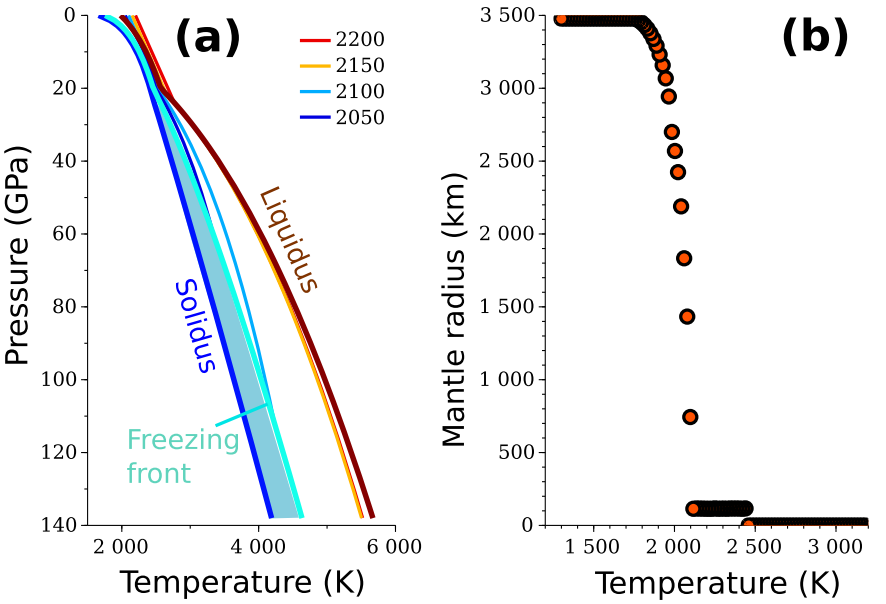

Figure 2. Thermal structure of the magma ocean. (a) Plot of the compiled solidus, liquidus, and the freezing front as functions of pressure. Also shown in the plot are four different geotherms. The potential temperature for each geotherm is indicated in the legend. (b) Plot of mantle radius a as a function of the potential temperature.

The geotherm within the MO follows an adiabat in regions where a single phase exists, i.e., above the liquidus or below the solidus temperatures. Within the partially molten zone, however, the geotherm should follow an isentropic path [*McKenzie*, 1984; *Asimow et al.*, 1997; *Stolper and Asimow*, 2007]. We present the detailed derivation of the thermal structure in supporting information section S3.4. From the thermal structure within the MO, we can describe the mantle radius a as a function of the potential temperature T.

We display the thermal structure within the MO for four different potential temperatures in Figure 2a. We also plot the liquidus, solidus, and the freezing front curves as functions of pressure. As the plots demonstrate, the isentrope within the partially molten region is marked by a different slope from the adiabat. The slope of the isentrope is weakly nonlinear and changes between different curves shown in the figure. The plot in panel b outlines the radius of the mantle, a, marked by the location of the intersection between the isentrope and the freezing front. To determine $\mathrm{d}a/\mathrm{d}T$ in equation (4), we fit the data in panel b with a piece wise polynomial curve, $a=a(T)$ (in m), given by,

$$a=\begin{cases} 0, & T>2100 \\ -1.18\times10^{-3}T^4+9.06T^3-2.6\times10^4T^2 & \\ +3.32\times10^7T-1.59\times10^{10}, & 1810<T\leq 2100 \\ 3.48\times10^6, & T\leq 1810 \end{cases}.$$

Using this expression, we evaluate $\mathrm{d}a/\mathrm{d}T$ analytically at each time step.

We use a fourth-order Runge-Kutta algorithm to integrate the ordinary differential equation (4). We use an adaptive time step method to ensure that the length of each time step is optimal to obtain a smooth solution of temperature and the resultant trapped melt fraction. Once the potential temperature is obtained for a time step, we use it to calculate the thermal structure and a as described above.

2.2.3. Chemical Evolution

We consider three reservoirs for each of the three volatile species, CO_2, H_2O, and N_2; the magma ocean (MO), the primitive atmosphere (PA), and the residual mantle (RM). As crystallization progresses, the initially liquid magma ocean is differentiated into a solid residual mantle and a gaseous primitive atmosphere. In the following formulation, we express the mass of volatile Z (H_2O, CO_2, or N_2) in reservoir B (MO, PA, and RM) as M_Z^B. The concentration of volatiles in each reservoir evolves, as the size of the reservoirs change.

We can write the total mass of volatile Z, M_Z^T, as a sum of the masses in the three reservoirs,

$$M_Z^T = M_Z^{MO} + M_Z^{PA} + M_Z^{RM}. \quad (6)$$

Owing to extremely low solubility of N_2 in solids, the last term in the right-hand side of equation (6) for N_2 is significantly smaller than the first two. As a result, we ignore this term in the equation for N_2.

As the MO crystallizes, the size of the reservoirs evolve. The mass of greenhouse volatiles (primarily CO_2) in the PA influence the cooling rate through the thermal emissivity in equation (4), coupling the thermal evolution with the chemical evolution. We present a detailed derivation of the equations governing the chemical evolution in supporting information.

2.3. Numerical Simulations

In this work, we carry out 360 numerical simulations of the thermal and chemical evolution. We conduct three series of simulations with initial H:C abundance ratios of 0.2, 0.3, and 0.4. In each series, the CO_2: N_2 ratio was fixed at 0.05, and the abundance of H_2O varied from 1 to 10 ocean masses, with the other volatiles masses set by the fixed ratios. For each of these 30 initial conditions, we carried out the calculations for both dynamic melt trapping and a constant 1% trapped melt fraction. Each of these simulations were repeated in five sets, varying the compaction time between 0.1 and 2.5 Ma. Additionally, we carried out another set of 60 numerical simulations for a constant compaction time of 0.5 Ma with the freezing rate numerically evaluated from the intersection of the linear freezing front and the adiabat. In this article, we report the results for a compaction time of 1.2 Ma unless stated otherwise. In all our numerical simulations, the initial mantle potential temperature is 3000 K.

3. Results

The results of our numerical simulations demonstrate that the volatile content of the residual mantle depends strongly on the competition between compaction within the freezing front and crystallization of the MO. For a compaction time of 1.2 Ma, the concentration of mantle volatiles is underestimated by nearly a factor of 14 when a constant trapped melt volume fraction is assumed. Our simulations also portray that the time to crystallization increases with an increase in the amount of CO_2 in the initial composition, up to approximately six ocean masses, at which point it takes ~3 Ma for the MO to fully crystallize. Details of these results are discussed next.

3.1. Evolution of Volatile Inventories

The evolution of the volatile content in the three reservoirs, MO, PA, and RM follow distinct trajectories. These trajectories are different for H_2O and CO_2. In the series of plots in Figures 3a and 3b we compare the evolution of the masses of these two volatiles in the three reservoirs. The H:C ratio for this set of simulations were 0.4, with an initial H_2O abundance of 10 ocean mass. In this simulation, the MO remains largely molten for the first 2.8 Ma. During this period, the majority of the CO_2 is partitioned into the primitive atmosphere, as the mass of CO_2 in the atmosphere is nearly 1.5 times higher than the MO. In contrast, nearly all of the initial H_2O remains trapped in the MO for the first 2.8 Ma. Since the MO is molten, the radius of the residual mantle is zero (panel d) during this period. The subsequent history of MO crystallization is marked by a steady nonlinear solidification of the MO over the next 700 ka. As a result of this solidification, the primitive atmosphere is enriched further in both H_2O and CO_2. Upon solidification, the atmospheric pressures of CO_2 and H_2O are ~3160 and ~1800 bars, respectively. Combined, these pressures are higher than the combined pressure of 3150 bars from the calculations of *Elkins-Tanton* [2008], for a 2000 km deep MO, containing 0.5 wt. % H_2O and 0.1 wt. % CO_2.

A hygrostat-like action of the freezing front can be observed by comparing the two curves for H_2O in Mantle in panel b. Contrary to the established models of constant trapped melt fraction plotted in broken lines, rapid solidification actually helps the mantle retain more volatiles, as a larger volume fraction of volatile-rich melt is trapped in the matrix according to our dynamic trapping model. This physical process is ignored in the model of constant trapped melt volume fraction, which leads to a volatile poor residual mantle. In panel b of both figures, we show the last 400 ka of the MO evolution when the distinction between the two models become most evident. The area between the curves for each reservoir is shaded red when the constant trapped melt fraction underestimates the volatile content in a given reservoir, and in green otherwise. As

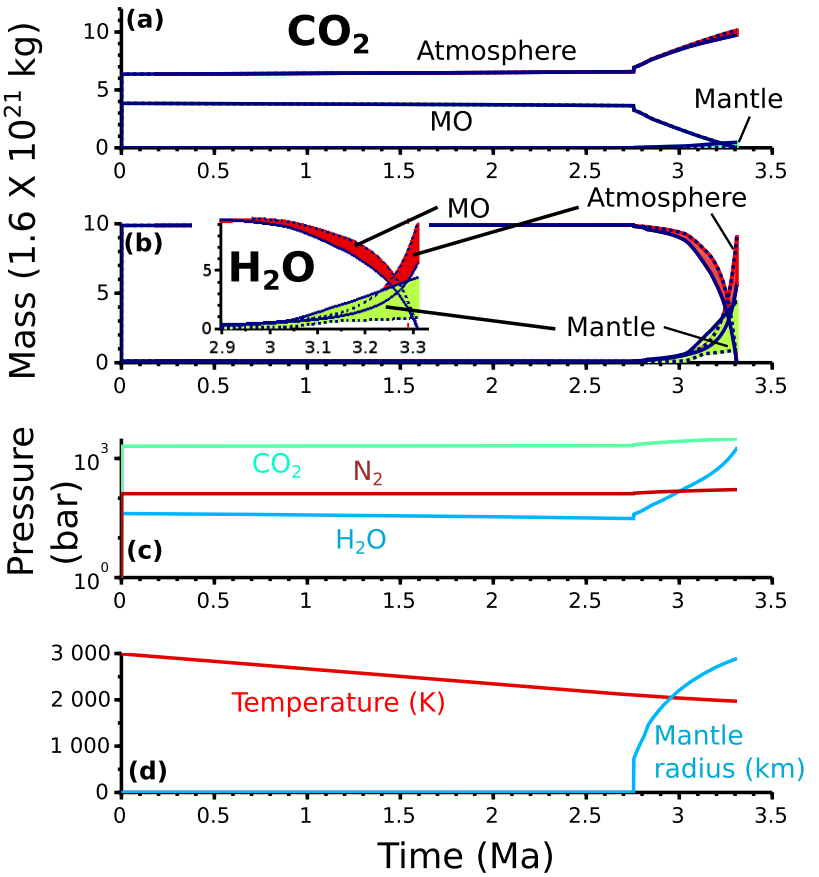

Figure 3. Evolution of the major volatile reservoirs. In these simulations, the initial volatile mass consisted of 10 oceans (1 ocean = 1.6×10^{21} kg) of H_2O in the initial BSE composition. The H:C ratio for the simulations was 0.4. The compaction time (τ) is ~1.2 Ma in these simulations. The masses of (a) CO_2 and (b) H_2O in the three reservoirs are compared. In both panels, solid curves correspond to simulations using dynamic trapping and broken curves correspond to constant trapped melt fraction. Shades of green and red represent excess and deficit of a volatile species in a reservoir with respect to the constant trapped melt fraction, respectively. (c) Partial pressure of each volatile species in the primitive atmosphere. (d) Evolution of the MO potential temperature (in red) and the mantle radius (in black).

the inset plots indicate, the amount of H_2O trapped in the mantle is underestimated by the model of constant melt volume fraction.

The abundance of CO_2 in the initial atmosphere plays a significant role in the duration of MO crystallization. In the evolution scenario in Figure 4, the initial CO_2 and N_2 abundances were 2 times lower than in Figure 3. During crystallization, the partial pressure of CO_2 in the atmosphere increases from ~1000 to ~1300 bars, substantially lower than in Figure 3. The lower CO_2 partial pressure in the atmosphere increases the crystallization rate, leading to the onset of solidification at 2.3 Ma. The partial pressure of the volatiles in these plots are also higher than the combined partial pressure of 240 bars resulting from the crystallization of a 2000 km deep MO containing 0.05 wt. % H_2O and 0.01 wt. % CO_2, estimated by *Elkins-Tanton* [2008]. The sharp contrast in the solidification time between these two figures demonstrates that within the range of radiative heat loss considered in this article, the greenhouse effect caused by CO_2 played a more dominant role in the crystallization time of the terrestrial MO than H_2O.

3.2. Volatile Concentration Upon Crystallization

Comparison between the estimates of CO_2 and H_2O concentrations in the current mantle and our predictions for the residual mantle reveals the important role played by dynamic melt trapping. These results are outlined in Figure 5. In the present day, two end-member compositions, the ocean island basalt (OIB) source and mid-oceanic ridge basalt (MORB) source are commonly used to constrain the volatile content of the mantle. The enriched OIB source likely contains 350–900 ppm H_2O and 400–800 ppm CO_2, compared to the modest concentrations of 50–150 ppm H_2O and 25–75 ppm CO_2 in the MORB source [*Hirschmann and*

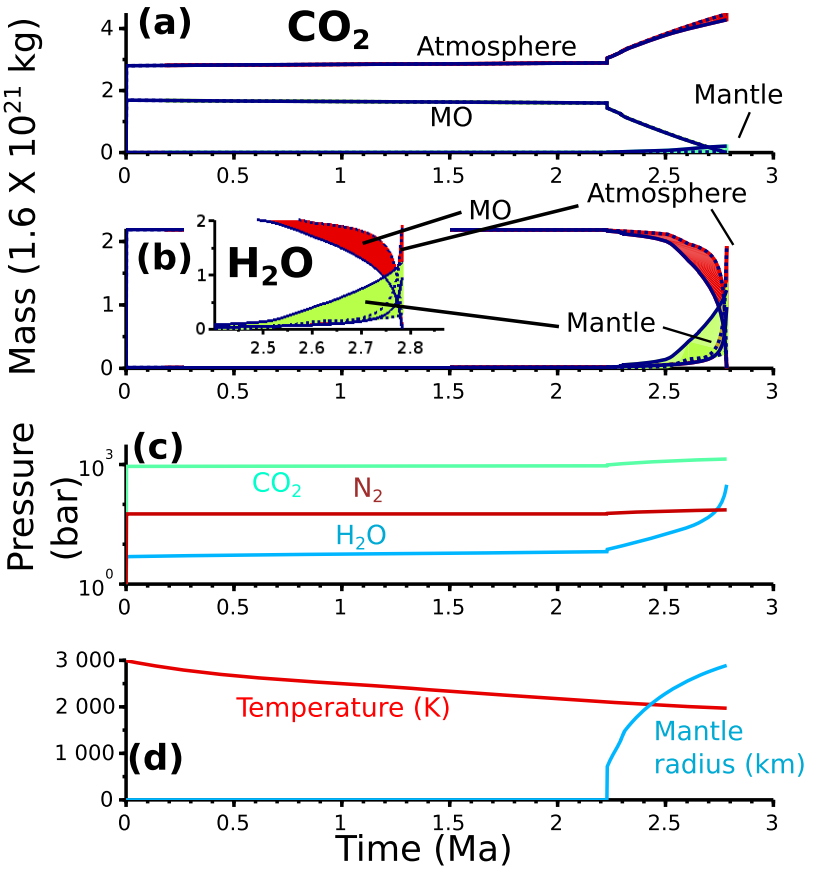

Figure 4. Evolution of the major volatile reservoirs, with an initial abundance of 2.2 ocean of H_2O in the BSE, and an H:C ratio of 0.2. The compaction time (τ) is ~1.2 Ma in these simulations. The masses of (a) CO_2 and (b) H_2O in the three reservoirs are compared. The shades and line colors have the same significance as in Figure 3. (c) Partial pressure of each volatile species in the primitive atmosphere. (d) Evolution of the MO potential temperature and the mantle radius.

Dasgupta, 2009]. The likely present-day mantle concentration of CO_2 and H_2O should have a value between these two end-members source regions.

The plots in Figure 5 compare the volatile concentration in the residual mantle immediately after crystallization from the MO for dynamic melt trapping (circles) and a constant trapped melt volume fraction of 1 vol. % (squares). All plots correspond to a compaction time of ~1.2 Ma. As the H_2O content in the BSE increases from 1 to 10 ocean masses (1 ocean mass = 1.6×10^{21} kg), the H_2O concentration in the residual mantle formed by dynamic melt trapping increases from ~200 to ~1300 ppm. For a constant trapped melt volume fraction, the same initial H_2O abundances produce a residual mantle containing ~40 and ~320 ppm H_2O, respectively. Dynamic melt trapping, therefore, leads to a mantle enriched in H_2O by a factor of 4–5. This effect is even more pronounced for CO_2, as illustrated by the plot in panel b. The residual mantle produced by dynamic melt trapping contains up to 14 times higher concentration of CO_2 compared to a mantle produced by constant melt trapping. The model of constant melt fraction fails to produce a residual mantle with CO_2 concentration somewhere between OIB and MORB source.

3.3. Evolution of Trapped Melt Fraction

An important outcome of dynamic melt trapping is the interaction between cooling rate and the amount of trapped melt fraction. Periods of rapid freezing are marked by large trapped melt fractions. The series of plots in Figure 6a depict the evolution of the trapped melt fraction for 28 different cases, with initial H_2O contents varying from 1 to 10 oceans and H:C ratios varying between 0.2 and 0.4. In each simulation, the trapped melt fraction increases steadily, in a nonlinear fashion with progressive crystallization of the MO. The horizontal line compares the constant trapped melt volume fraction of 0.01 with the dynamic

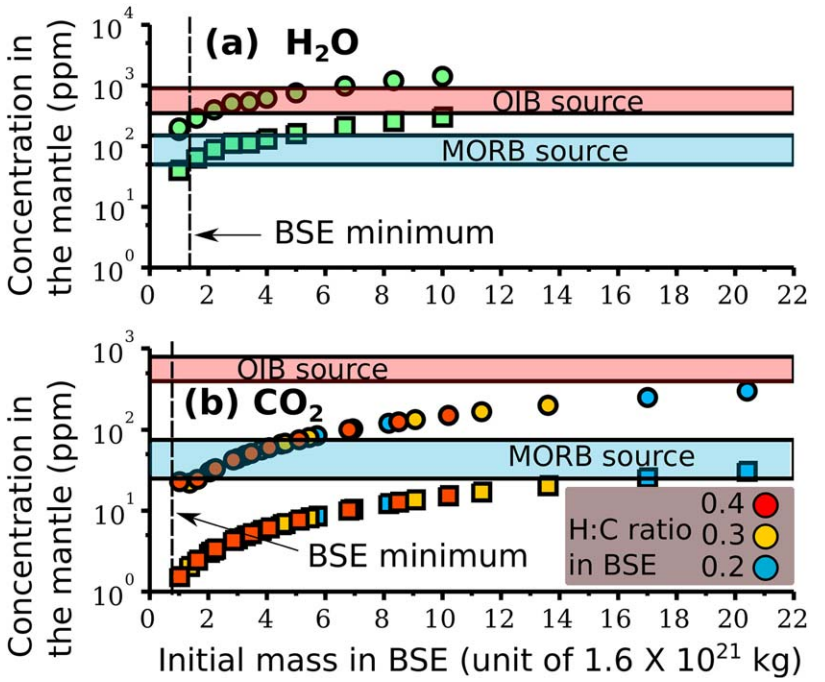

Figure 5. Final concentration of (a) H_2O and (b) CO_2 in the residual mantle. Circles indicate data from numerical experiments with dynamic melt trapping while filled squares indicate data from models with a constant trapped melt volume fraction. The compaction time (τ) is ~1.2 Ma in these simulations.

melt volume fractions. The plot in Figure 6b shows the time to complete solidification of the magma ocean as a function of CO_2 content (in units of ocean mass, 1.6×10^{21} kg). As the mass of CO_2 in the BSE increases from one to seven oceans, the surface heat flux decreases due to increasing greenhouse effect, increasing the time of complete solidification in a nonlinear fashion. For larger CO_2 content in the BSE, the solidification time becomes insensitive to CO_2 content saturating at a value of ~3 Ma. For a given CO_2 content, the solidification time is insensitive to the H:C ratio, since the influence of H_2O on the thermal emissivity is much weaker than CO_2.

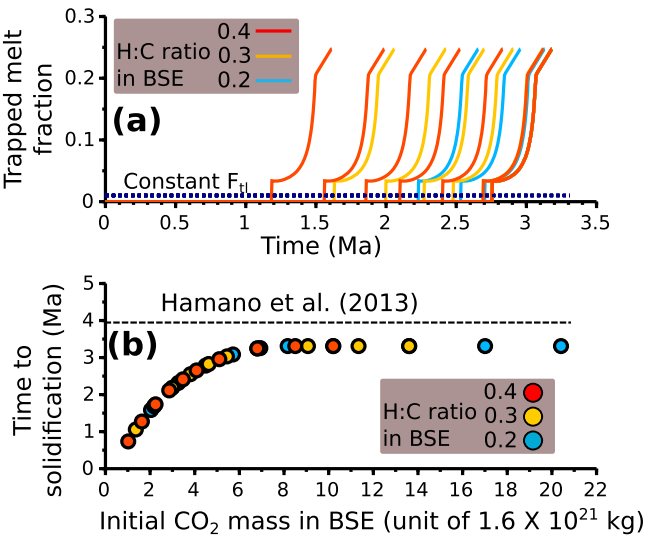

Figure 6. (a) Evolution of trapped melt fraction and (b) time to complete crystallization of the magma ocean. The compaction time (τ) is ~1.2 Ma in these simulations. In Figure 6a the stars corresponding to jumps in the trapped melt fraction reflect rapid freezing in the lower mantle and near the transition zone. Results from three sets of simulations are presented. In each of these sets of simulations, corresponding to a distinct H:C ratio in the BSE, the total H_2O content varied between one and ten oceans of water (1.6×10^{21} kg). The broken horizontal line in Figure 6b corresponds to the time of complete MO solidification from *Hamano et al.* [2013].

The volatile content of the solidifying mantle is substantially influenced by dynamic melt trapping. Since this is the cumulative total of the volatile content of the residual mantle, it increases monotonically with time. The plots in Figure 7 compares the evolution of concentrations of H_2O and CO_2 in the mantle for both dynamic melt trapping and a constant trapped melt fraction of 0.01. The concentration of CO_2 and H_2O in the solidifying mantle is defined as the mass of the volatile species in the solidifying mantle divided by the mass of the solidified mantle.

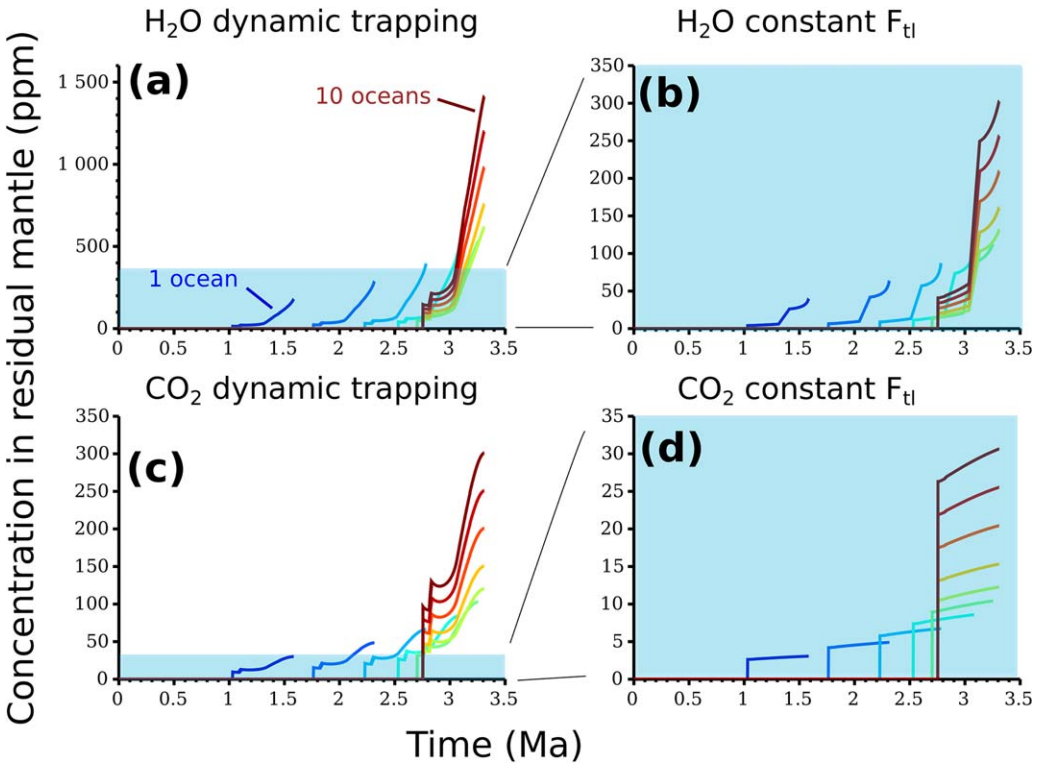

Figure 7. Evolution of volatile concentration in the solidifying mantle. The plot compares the evolution for both dynamic melt trapping and a constant trapped melt fraction of 0.01. The compaction time (τ) is $\sim$1.2 Ma in these simulations. Different curves correspond to the initial H_2O abundance in the BSE, which varied from 1 to 10 oceans (1.6×10^{21} kg). The initial CO_2 abundance in the BSE is set by the H:C ratio of 0.2. Heights of the shaded regions in Figures 7a and 7c span the entire height of Figures 7b and 7d.

4. Discussion

4.1. Assumptions in This Model and Comparison With Previous Thermal Models

During the MO crystallization, fractionation of major elements is likely to take place, although *Solomatov and Stevenson* [1993a] argue that convective suspension of the crystals will prevent the melt from following a fractional crystallization path. If operative, fractionation of major elements between the residual mantle and the MO can influence the evolution by changing the temperature of the solidus as crystallization progresses, changing the solubility of volatiles in the solid mineral phases [*Zhao et al*., 2004], and by rendering the upper part of the residual mantle denser, prone to subsolidus convective overturn subsequent to complete crystallization of the MO [*Elkins-Tanton et al*., 2003]. In addition, the presence of volatiles will reduce the solidus and liquidus temperatures [e.g., *Katz et al*., 2003; *Dasgupta and Hirschmann*, 2006; *Nomura et al*., 2011, 2014], resulting in the beginning of crystallization at a later stage of cooling.

The effects arising from major element fractionation and depression of the solidus and the liquidus will result in a complex set of processes resulting in a more complex set of coupling between volatile storage, melt expulsion from the freezing front, and MO crystallization. In this article, we do not account for these effects. Instead, we chose to focus on a model dry solidus to identify the first order effects of compaction on volatile trapping. Future work incorporating the more complex chemical effects will be extremely useful in obtaining tighter bounds on the volatile concentration.

The issue of magma ocean crystallization has been discussed in a number of previous numerical models [*Abe*, 1997; *Abe and Matsui*, 1988; *Solomatov and Stevenson*, 1993b,a,c; *Elkins-Tanton*, 2008; *Hamano et al*., 2013; *Lebrun et al*., 2013; *Monteux et al*., 2016]. Of these articles, the works of *Abe and Matsui* [1988], *Elkins-Tanton* [2008], *Hamano et al*. [2013], and *Lebrun et al*. [2013] explicitly deal with the feedback between a volatile-rich protoatmosphere and the rate of MO crystallization. The results in this article extend these results by incorporating the feedback between volatile concentrations in the MO and the rate of cooling, and its effect on the volatile concentration in the residual mantle. As discussed earlier, the results of

atmospheric pressure and crystallization times from our work agree well with the recent models by *Elkins-Tanton* [2008] and *Hamano et al.* [2013]. The final atmospheric pressure in all of these studies, including ours, is substantially higher than the initial model of *Abe and Matsui* [1988]. In addition, an important difference between the models incorporating the effect of a greenhouse atmosphere and those without, is the timing of MO crystallization. For example, the model of *Monteux et al.* [2016] suggests complete MO crystallization takes place within 20 ka, substantially lower than the estimates of a few Ma in this work and those of *Hamano et al.* [2013]. This difference outlines the crucial role played by a greenhouse atmosphere and neglecting this effect can lead to substantial underestimation of MO crystallization time and its implications for the early evolution of the Earth. Finally, unlike the model of *Lebrun et al.* [2013], we do not consider the effect of radiogenic heating. Radiogenic heating is usually neglected in MO crystallization models as the half-lives of the majority of the heat producing elements are longer than MO crystallization time scales. Due to the presence of short-lived radiogenic isotopes in the early Earth, however, the relatively long Mo crystallization models can be influenced by radiogenic heating. This issue needs to be investigated further in future models.

4.2. Sensitivity Tests

The primary outcome of the magma ocean crystallization and compaction model is the mass of volatiles in the residual mantle and primitive atmosphere following the crystallization. The thermal and chemical evolution model explored here differs from previous calculations because it incorporates a parameterization of the trapped melt fraction as a function of the rates of compaction within the freezing front and the rate of crystallization of the magma ocean (or the rate of propagation of the freezing front). It is, therefore, important to assess the influence of these parameters on the final volatile concentration in the mantle. One key parameter in our model is the compaction time, τ, the characteristic time scale for effective segregation of melt through the compacting layer.

To test the influence of compaction time on the final concentration of H_2O and CO_2 in the residual mantle, we carried out a series of numerical simulations where we varied the value of τ between 0.1 and 2.5 Ma. The results of the models are displayed in Figure 8.

For a given initial mass, the final concentration of both H_2O and CO_2 in the mantle increase with an increase in compaction time. Longer compaction times result in slow expulsion of melt from the freezing front. Consequently, a larger volume of melt is trapped in the freezing front also trapping a larger amount of dissolved volatiles. The map in Figure 8 illustrates the variations in the final concentration of dissolve H_2O and CO_2 in the residual mantle as a function of initial volatile abundance and the compaction time. For a given initial volatile abundance, the final mantle H_2O concentration is reduced by approximately a factor of 5 due to a reduction in the compaction time by a factor of 25. The final concentration of CO_2 is reduced is by a factor of 15 for the same reduction in compaction time.

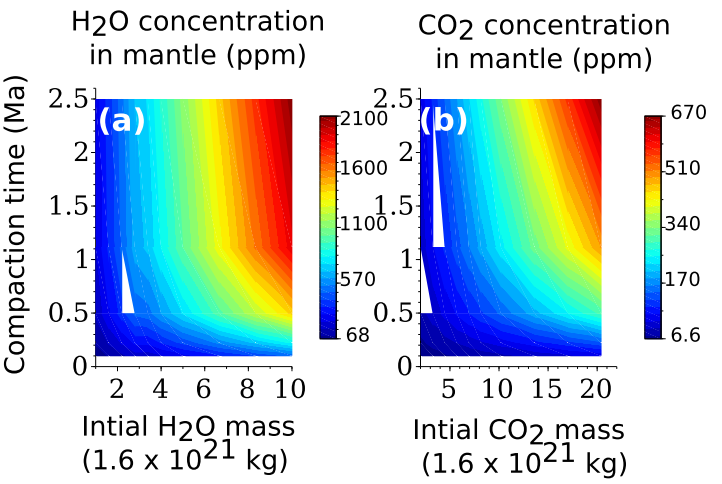

Figure 8. A map of final concentrations (in ppm) of H_2O and CO_2 in the residual mantle after solidification as a function of compaction time and initial volatile content in the BSE.

The sensitivity tests presented above demonstrate that the final volatile concentration in the residual mantle is strongly sensitive to the time of compaction. The compaction time is the ratio between the thickness of the compacting layer (or the freezing front in this case) and the average velocity of matrix sedimentation. While a large compaction length will increase the time of compaction, leading to a larger trapped volatile concentration in the residual mantle, the influence of a larger matrix sedimentation velocity will be the opposite. We chose

to report results for a compaction time of ~1.2 Ma. The calculations presented in the supplement indicate that the characteristic compaction time for these simulations is 4.35 Ma. The estimate of the final volatile concentration in the mantle (for a compaction time of 1.2 Ma), therefore, provides a conservative estimate of trapped volatiles. These results also identify the shortcoming of previous thermochemical models of magma ocean solidification for quantifying the mantle volatile content, as they overestimate the efficiency of compaction.

4.3. Volatile Retention and H:C Ratio

One mechanism for creating early volatile reservoirs in the mantle is the crystallization of the magma ocean. We can compare the H:C ratios from our simulations with the available geochemical estimates for mantle H:C ratios to identify the effectiveness of magma ocean crystallization in the relative sequestration of H and C in the early mantle.

Since H is more soluble in magmas than C (at least under the relatively oxidizing conditions at which H_2O and CO_2 are the principle magmatic volatiles [e.g., *Elkins-Tanton*, 2008]), the residual mantle, upon crystallization, should accumulate more H dissolved in the trapped melt, increasing the H:C ratio above the initial values. This preferential retention of H in the crystallizing mantle may account for the mantle's high H:C ratio (between 0.5 and 0.75) [*Hirschmann and Dasgupta*, 2009] compared to chondrites (generally <0.3) [*Kerridge*, 1985].

Our results identify the differences in the degree of C enrichment of the mantle due to dynamic melt trapping, as outlined in Figure 9a. This plot of H:C ratio of the residual mantle as a function of the compaction time illustrates a nonlinear decrease in the H:C ratio with an increase in the compaction time (data points in solid circles). The data in solid squares represent the H:C ratio of the residual mantle resulting from crystallization with 1 vol. % trapped melt. The H:C ratio in this set of simulations remain at a constant level of 5.7. In these simulations, the initial H:C ratio of the BSE was 0.2. Extrapolating our results, a higher compaction time could lead to further reduction of the H:C ratio. In addition, other processes can also explain the differences between our predicted H:C ratios for the early mantle and the estimates for the present-day mantle.

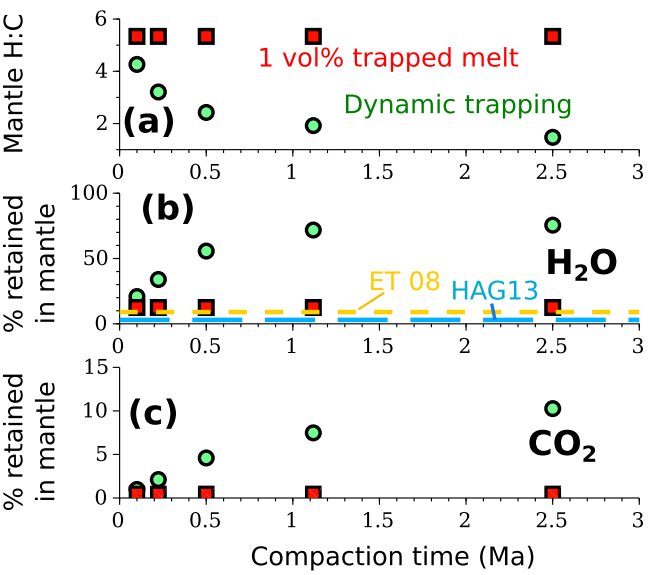

Figure 9. A comparison between volatile ratios in the residual mantle. The calculations are carried out for an initial H:C ratio of 0.2 in the BSE and an initial H_2O mass of 1.6 oceans (2.56×10^{21} kg). (a) Plot of H:C ratio in the residual mantle as a function of compaction time. Circles represent models with dynamic melt trapping, squares represent models with a constant trapped melt volume fraction of 1%. (b) Retention of initial H_2O content of the BSE in the residual mantle upon crystallization. The line marked ET08 is the estimate of H_2O retained by the crystallization of a 2000 km thick magma ocean, initially containing 0.5 wt. % H_2O by *Elkins-Tanton* [2008]. The line marked HAG13 is the estimate provided by [*Hamano et al.*, 2013, Figure 3a]. (c) The wt. % of initial CO_2 retained in the residual mantle as a function of compaction time.

Our calculations do not account for the possibility of additional C being sequestered in the mantle by proposed C-pumping effects [*Hirschmann*, 2012; *Dasgupta et al.*, 2013] or for modification of the mantle H:C ratio by processes subsequent to magma ocean solidification. Also, the relative proportions of H and C sequestered will be sensitive to oxygen fugacity, which affects relative volatile solubilities [e.g., *Hirschmann et al.*, 2012; *Stanley et al.*, 2014]. Comparison between available geochemical estimates and our H:C ratios indicate that this is a dimension worthy of further exploration in future models.

The fraction of volatiles retained in the mantle are strongly influenced by the compaction time. The plots in Figures 9b and 9c compare the fraction of initial H_2O and CO_2 retained in the mantle as a function of the compaction time. As the plots indicate, with an increase in the compaction time from 0.1 to 2.5 Ma, the wt. % of retained H_2O and CO_2 increase from 19 and 0.8

to 77 and 12%, respectively. The mantle crystallizing by 1 vol. % melt trapping retains 13% water, similar to the estimate by *Elkins-Tanton* [2008], but higher than the estimate of 3% by *Hamano et al*. [2013].

5. Conclusions

In this article, we demonstrate that compaction within the freezing front of a crystallizing MO is relatively inefficient, with matrix compaction velocities 2–3 orders of magnitude smaller than the typical velocities of MO freezing front advancement. We propose that the trapped melt volume fraction in the MO freezing front is dynamically controlled by the ratio between the rate of MO freezing and the rate of compaction within the freezing front. We demonstrate that the residual mantle resulting from crystallization from an MO can contain considerable amounts of volatiles owing to melt trapped by the inefficiency of compaction. In the simulations that assume the longest compaction time and considerable initial volatile abundance, the residual mantle contains more than 2200 and 740 ppm CO_2.

Acknowledgments
The authors gratefully acknowledge insightful reviews and comments from two anonymous reviewers, Constantin Sandu, and editor Thorsten Becker. The research by MMH was supported by NSF AST1344133 and NASA NNX11AG64. SH-M acknowledges travel support from NSF EAR1215800. The source code for simulations is available via open access at https://doi.org/10.5281/zenodo.824413.

References

Abe, Y. (1997), Thermal and chemical evolution of the terrestrial magma ocean, *Phys. Earth Planet. Inter.*, *100*, 27–39.
Abe, Y., and T. Matsui (1988), Evolution of an impact-generated H_2O-CO_2 atmosphere and the formation of a hot protoocean in the earth, *J. Atmos. Sci.*, *45*(21), 3081–3101.
Asimow, P. D., M. M. Hirschmann, and E. M. Stolper (1997), An analysis of variations in isentropic melt productivity, *Philos. Trans. R. Soc. A*, *355*(1723), 255–281.
Bell, E. A., P. Boehnke, T. M. Harrison, and W. L. Mao (2015), Potentially biogenic carbon preserved in a 4.1 billion-year-old zircon, *Proc. Natl. Acad. Sci. U. S. A.*, *112*, 14,518–14,521, doi:10.1073/pnas.1517557112.
Bercovici, D., Y. Ricard, and G. Schubert (2001), A two-phase model for compaction and damage: 1. General theory, *J. Geophys. Res.*, *106*(5), 8887–8906.
Bolfan-Casanova, N. (2000), Water partitioning between nominally anhydrous minerals in the MgO–SiO2–H2O system up to 24 GPa: Implications for the distribution of water in the Earth's mantle, *Earth Planet. Sci. Lett.*, *182*(3–4), 209–221, doi:10.1016/S0012-821X(00)00244-2.
Bolfan-Casanova, N. (2002), Pressure dependence of H solubility in magnesiowüstite up to 25 GPa: Implications for the storage of water in the Earth's lower mantle, *Geophys. Res. Lett.*, *29*(10), 1–4, doi:10.1029/2001GL014457.
Cawthorn, R., and F. Walraven (1998), Emplacement and crystallization time for the Bushveld Complex, *J. Petrol.*, *39*(9), 1669–1687, doi:10.1093/petrology/39.9.1669.
Dasgupta, R., and M. M. Hirschmann (2006), Melting in the earth's deep upper mantle caused by carbon dioxide, *Nature*, *440*, 659–662, doi:10.1038/nature04612.
Dasgupta, R., and M. M. Hirschmann (2010), The deep carbon cycle and melting in Earth's interior, *Earth Planet Sci. Lett*, *298*, 1–13, doi:10.1016/j.epsl.2010.06.039.
Dasgupta, R., A. Mallik, K. Tsuno, A. C. Withers, G. Hirth, and M. M. Hirschmann (2013), Carbon-dioxide-rich silicate melt in the Earth's upper mantle, *Nature*, *493*(7431), 211–215, doi:10.1038/nature11731.
Elkins-Tanton, L. (2008), Linked magma ocean solidification and atmospheric growth for earth and mars, *Earth Planet. Sci. Lett.*, *271*, 181–191, doi:10.1016/j.epsl.2008.03.062.
Elkins-Tanton, L. T., E. M. Parmentier, and P. C. Hess (2003), Magma ocean fractional crystallization and cumulate overturn in terrestrial planets: Implications for mars, *Meteoritics Planet. Sci.*, *38*(12), 1753–1771.
Halliday, A. N. (2013), The origins of volatiles in the terrestrial planets, *Geochim. Cosmochim. Acta*, *105*, 146–171, doi:10.1016/j.gca.2012.11.015.
Hamano, K., Y. Abe, and H. Genda (2013), Emergence of two types of terrestrial planet on solidification of magma ocean, *Nature*, *497*(7451), 607–610, doi:10.1038/nature12163.
Hayes, J. M., and J. R. Waldbauer (2006), The carbon cycle and associated redox processes through time, *Philos. Trans. R. Soc. B*, *361*(1470), 931–950, doi:10.1098/rstb.2006.1840.
Hier-Majumder, S., and B. Tauzin (2017), Pervasive upper mantle melting beneath the western US, *Earth Planet. Sci. Lett.*, *463*, 25–35, doi:10.1016/j.epsl.2016.12.041.
Hier-Majumder, S., Y. Ricard, and D. Bercovici (2006), Role of grain boundaries in magma migration and storage, *Earth Planet. Sci. Lett.*, *248*(3–4), 735–749, doi:10.1016/j.epsl.2006.06.015.
Hirschmann, M. M. (2006), Water, melting, and the deep earth H_2O cycle, *Annu. Rev. Earth Planet. Sci.*, *34*(1), 629–653, doi:10.1146/annurev.earth.34.031405.125211.
Hirschmann, M. M. (2012), Magma ocean influence on early atmosphere mass and composition, *Earth Planet. Sci. Lett.*, *341–344*, 48–57, doi:10.1016/j.epsl.2012.06.015.
Hirschmann, M. M., and R. Dasgupta (2009), The H/C ratios of Earth's near-surface and deep reservoirs, and consequences for deep Earth volatile cycles, *Chem. Geol.*, *262*(1–2), 4–16, doi:10.1016/j.chemgeo.2009.02.008.
Hirschmann, M. M., A. C. Withers, P. Ardia, and N. T. Foley (2012), Solubility of molecular hydrogen in silicate melts and consequences for volatile evolution of terrestrial planets, *Earth Planet. Sci. Lett.*, *345–348*, 38–48, doi:10.1016/j.epsl.2012.06.031.
Irvine, T. (1980), Magmatic infiltration metasomatism, double-diffusive fractional crystallisation, and adcumulus growth in the muskox intrusion and other layered in-trusions, in *Physics of Magmatic Processes*, edited by R. Hargraves, pp. 325–383.
Katz, R. F., M. Spiegelman, and C. H. Langmuir (2003), A new parametrization of hydrous mantle melting, *Geochem. Geophys. Geosyst.*, *4*, 1073, doi:10.1029/2002GC000433.
Kerridge, J. F. (1985), Carbon, hydrogen and nitrogen in carbonaceous chondrites: Abundances and isotopic compositions in bulk samples, *Geochim. Cosmochim. Acta*, *49*, 1707–1714, doi:10.1016/0016-7037(85)90141-3.
Lebrun, T., H. Massol, E. Chassefière, A. Davaille, E. Marcq, P. Sarda, F. Leblanc, and G. Brandeis (2013), Thermal evolution of an early magma ocean in interaction with the atmosphere, *J. Geophys. Res. Planets*, *118*, 1155–1176, doi:10.1002/jgre.20068.

Marty, B. (2012), The origins and concentrations of water, carbon, nitrogen and noble gases on Earth, *Earth Planet. Sci. Lett.*, *313–314*, 56–66, doi:10.1016/j.epsl.2011.10.040.
McGovern, P. J., and G. Schubert (1989), Thermal evolution of the Earth: Effects of volatile exchange between atmosphere and interior, *Earth Planet. Sci. Lett.*, *96*, 27–37.
McKenzie, D. (1984), The generation and compaction of partially molten rock, *J. Petrol.*, *25*, 713–765.
McKenzie, D. (2011), Compaction and crystallization in magma chambers: Towards a model of the Skaergaard intrusion, *J. Petrol.*, *52*(5), 905–930, doi:10.1093/petrology/egr009.
Monteux, J., D. Andrault, and H. Samuel (2016), On the cooling of a deep terrestrial magma ocean, *Earth Planet. Sci. Lett.*, *448*, 140–149, doi:10.1016/j.epsl.2016.05.010.
Nomura, R., H. Ozawa, S. Tateno, K. Hirose, J. Hernlund, S. Muto, H. Ishii, and N. Hiraoka (2011), Spin crossover and iron-rich silicate melt in the Earth's deep mantle, *Nature*, *473*(7346), 199–202, doi:10.1038/nature09940.
Nomura, R., K. Hirose, K. Uesugi, Y. Ohishi, A. Tsuchiyama, A. Miyake, and Y. Ueno (2014), Low core-mantle boundary temperature inferred from the solidus of pyrolite, *Science*, *343*(6170), 522–525, doi:10.1126/science.1248186.
Rudge, J. F., D. Bercovici, and M. Spiegelman (2011), Disequilibrium melting of a two phase multicomponent mantle, *Geophys. J. Int.*, *184*, 699–718, doi:10.1111/j.1365-246X.2010.04870.x.
Rüpke, L., J. Phipps Morgan, M. Hort, and J. A. D. Connolly (2004), Serpentine and the subduction zone water cycle, *Earth Planet. Sci. Lett.*, *223*, 17–34, doi:10.1016/j.epsl.2004.04.018.
Scott, T., and D. Kohlstedt (2006), The effect of large melt fraction on the deformation behavior of peridotite, *Earth Planet. Sci. Lett.*, *246*(3–4), 177–187.
Shcheka, S. S., M. Wiedenbeck, D. J. Frost, and H. Keppler (2006), Carbon solubility in mantle minerals, *Earth Planet. Sci. Lett.*, *245*(3–4), 730–742, doi:10.1016/j.epsl.2006.03.036.
Sleep, N. H., and K. Zahnle (2001), Carbon dioxide cycling and implications for climate on ancient Earth, *J. Geophys. Res.*, *106*, 1373–1399, doi:10.1029/2000JE001247.
Snyder, G. A., L. A. Taylor, and C. R. Neal (1992), A chemical model for generating the source of mare basalts: Combined equilibrium and fractional crystallization of the lunar magmasphere, *Geochim. Cosmochim. Acta*, *56*, 3809–3823.
Solomatov, V. S., and D. J. Stevenson (1993a), Nonfractional crystallization of a terrestrial magma ocean, *J. Geophys. Res.*, *98*(E3), 5391–5406.
Solomatov, V. S., and D. J. Stevenson (1993b), Suspension in convective layers and style of differentiation of a terrestrial magma ocean, *J. Geophys. Res.*, *98*(E3), 5375–5390.
Solomatov, V. S., and D. J. Stevenson (1993c), Kinetics of crystal growth in a terrestrial magma ocean, *J. Geophys. Res.*, *98*(E3), 5407–5418.
Stanley, B. D., M. M. Hirschmann, and A. C. Withers (2014), Solubility of COH volatiles in graphite-saturated martian basalts, *Geochim. Cosmochim. Acta*, *129*, 54–76, doi:10.1016/j.gca.2013.12.013.
Stolper, E., and P. Asimow (2007), Insights into mantle melting from graphical analysis of one-component systems, *Am. J. Sci.*, *307*(8), 1051–1139, doi:10.2475/08.2007.01.
Suckale, J., J. A. Sethian, J.-d. Yu, and L. T. Elkins-Tanton (2012), Crystals stirred up: 1. Direct numerical simulations of crystal settling in non-dilute magmatic suspensions, *J. Geophys. Res.*, *117*, E08004, doi:10.1029/2012JE004066.
Takei, Y., and S. Hier-Majumder (2009), A generalized formulation of interfacial tension driven fluid migration with dissolution/precipitation, *Earth Planet. Sci. Lett.*, *288*(1–2), 138–148, doi:10.1016/j.epsl.2009.09.016.
Tegner, C., P. Thy, M. B. Holness, J. K. Jakobsen, and C. E. Lesher (2009), Differentiation and compaction in the Skaergaard intrusion, *J. Petrol.*, *50*(5), 813–840, doi:10.1093/petrology/egp020.
Wager, L. R. (1960), The major element variation of the layered series of the Skaergaard intrusion and a re-estimation of the average composition of the hidden layered series and of the successive residual magmas, *J. Petrol.*, *1*, 364–398.
Wimert, J. T., and S. Hier-Majumder (2012), A three-dimensional microgeodynamic model of melt geometry in the earth's deep interior, *J. Geophys. Res.*, *117*, B04203, doi:10.1029/2011JB009012.
Zhao, Y., S. Ginsberg, and D. Kohlstedt (2004), Solubility of hydrogen in olivine: Dependence on temperature and iron content, *Contrib. Mineral. Petrol.*, *147*, 155–161.